

Ionic Liquid-based electroactive materials: a novel approach for cardiac tissue engineering strategies

R.M. Meira^{1,2}, D.M. Correia^{1,3}, A. García Díez⁴, S. Lanceros-Mendez^{4,5}, C. Ribeiro^{1,2,*}

¹Physics Centre of Minho and Porto Universities (CF-UM-UP), University of Minho, 4710-057 Braga, Portugal

²LaPMET - Laboratory of Physics for Materials and Emergent Technologies, University of Minho, 4710-057 Braga, Portugal

³Centre of Chemistry, University of Trás-os-Montes e Alto Douro, 5000-801 Vila Real, Portugal

⁴BCMaterials, Basque Center for Materials, Applications and Nanostructures, UPV/EHU Science Park, 48940 Leioa, Spain

⁵IKERBASQUE, Basque Foundation for Science, 48013 Bilbao, Spain

*corresponding author: cribeiro@fisica.uminho.pt

Abstract: Cardiac tissue regeneration strategies are increasingly taking advantage of electroactive scaffolds to actively recreate tissue microenvironment. In this context, this work reports on advanced materials based on two different ionic liquids (ILs), 2-hydroxyethyl-trimethylammonium dihydrogen phosphate ([Ch][DHP]) and choline bis(trifluoromethylsulfonyl)imide ([Ch][TFSI]), combined with poly(vinylidene fluoride-co-trifluoroethylene) (P(VDF-TrFE)) for the development of ionic electroactive IL/polymer hybrid materials for cardiac tissue engineering (TE). The morphological, physico-chemical, thermal and electrical properties of the hybrid materials, as well as their potential use as scaffolds for cardiac TE applications were evaluated. Besides of inducing changes in the surface topography, roughness and wettability of the composites, the incorporation of [Ch][DHP] and [Ch][TFSI] allows to increase surface (σ_{surface}) and volume (σ_{volume}) electrical conductivity. Further, washing the hybrid samples with phosphate-buffered saline solution strongly decreases the σ_{surface} , whereas σ_{surface} and σ_{volume} of the composites remains almost unaltered after exposure to ultraviolet sterilization treatment. Additionally, it is verified that the IL incorporation influences the P(VDF-TrFE) microstructure and crystallization process, acting as defect during its crystallization. Cytotoxicity assays revealed that just [Ch][DHP] based hybrid films are not cytotoxic. These films also support H9c2 myoblast cell adhesion and proliferation,

demonstrating their suitability for cardiac TE strategies based on electroactive microenvironments.

Keywords: composites, choline-based ionic liquids, P(VDF-TrFE), cardiac tissue engineering

1. Introduction

Cardiovascular diseases are one of the major causes of death and disability throughout the world. In spite of the notable progress in treatment strategies, existing treatments, which involves pharmacological and surgical intervention, are still unable to restore the cardiac function of the damaged myocardium^{1,2}. Moreover, these treatments have limited effects to cure patients with end-state heart failure³. In what patients with end-state heart failure is concerned, heart transplantation is still the only curative treatment option, notwithstanding the risks associated with this surgical procedure, such as heart transplant rejection, and limitations such as the shortage of organ donors^{3,4}. Endeavours have been carried out to develop more effective and less invasive therapeutic strategies for myocardial regeneration.

Current studies in regenerative medicine are taking advantage of tissue engineering (TE) to develop functional cardiac muscle constructs to repair or replace damaged and injured cardiac muscle tissue^{5,6}. To achieve this goal, TE uses biologically bioactive factors, cells and scaffolds, being scaffolds a key element on TE strategies since they can be designed to provide structural support, while giving the necessary biochemical and biophysical cues to cells in order to promote their growth and differentiation into desired tissue^{7,8}. Besides of being biocompatible, an ideal scaffold for cardiac tissue engineering should possess the following requirements: (i) it must have a similar structure to the native cardiac tissue; (ii) present suitable surface properties (surface charge, surface chemistry, surface topography and surface wettability) to promote cell attachment, proliferation and differentiation; and (iii) should be mechanically stable and possess electrical and mechanical properties close to those of the native cardiac tissue to enable the propagation of electrical signals, essential for continuous and synchronized tissue contraction^{9,10}.

In recent years, efforts have been devoted to develop scaffolds for cardiac TE aiming the aforementioned requirements. Naturally-derived materials, such as alginate^{11,12}, collagen^{13,14}, chitosan^{15,16}, and hyaluronic acid (HA)^{17,18}, have been explored for the

development of scaffolds for cardiac TE mainly due to their biocompatibility, biodegradability and extracellular matrix (ECM) mimicking ability^{10,19}. However, these materials show poor mechanical and electrical properties, as well as rapid degradation kinetics, which limits their use^{1,10}. Thus, a wide variety of synthetic polymers, such as poly(ethylene glycol) (PEG)²⁰ and poly(caprolactone) (PCL)²¹, arise as alternative materials as they display tailored physicochemical properties and possess superior mechanical properties than those of natural origin, even though they show lower affinity for cellular adhesion due to their lack of cell adhesion sites^{1,10}. To address this issue, the surface of synthetic scaffolds is often functionalized with ECM proteins, such as collagen or gelatin, or modified by plasma treatments to enhance cell adhesion and proliferation⁵. Conductive materials such as carbon nanotubes (CNTs), gold nanoparticles (AuNPs), polyaniline (PANI) and polypyrrole (PPy) have been also widely used in cardiac TE applications as reinforcing material, allowing the development of active scaffolds capable of electrically stimulate cells^{22,23}. However, they require wiring and an external power source²⁴. Conversely, specific active materials, such as piezoelectric ones, have the ability to mimic the natural cell microenvironment by providing not only the structural support that cells require, but also the necessary electrical and/or mechanical stimuli to promote cell proliferation and differentiation into a specific tissue without the need of an external voltage source, making them attractive materials for applications toward TE^{8,24}. Piezoelectric polymers, such as poly(lactic-co-glycolic acid) (PLGA)^{25,26}, poly(L-lactic acid) (PLLA)^{27,28} and poly(vinylidene fluoride-co-trifluoroethylene) (P(VDF-TrFE))^{29,30}, have been implemented in the development of active scaffolds for cardiac TE applications. Among piezoelectric polymers, poly(vinylidene fluoride) (PVDF) and its copolymers, as P(VDF-TrFE), are the ones that stand out the most due to their chemical resistance, good mechanical properties and excellent electroactive properties: piezoelectric, pyroelectric and ferroelectric properties and high dielectric constant³¹. Moreover, these biocompatible piezoelectric polymers are easily tailored in terms of structure and morphology, which allow them to be processed into different morphologies/structures, including films and porous films, 3D scaffolds, fibers or spheres³².

With respect to PVDF, this semi-crystalline polymer can crystallize into five distinct crystalline phases (α , β , δ , γ , and ϵ) depending on the processing method, being the β -phase the most relevant one for sensor and actuator applications based on its high electroactive (piezo-, pyro- and ferroelectric) response³¹. Different processing strategies

have been developed to obtain PVDF in this electroactive phase³³, one of them being the development of copolymers such as P(VDF-TrFE), that for specific VDF contents crystallizes directly in the electroactive β -phase regardless of the processing method³³. Thus, P(VDF-TrFE) has been chosen to develop this work.

Further, the incorporation of specific fillers into PVDF, such as magnetic nanoparticles³⁴, carbonaceous fillers³⁵ and more recently ionic liquids (ILs)^{36, 37}, has enabled the development of PVDF-based composites for TE applications with improved properties and/or new functionalities. In particular, ILs have gained special recent attention in this scope based on their electrochemical and thermal stability, high ionic conductivity and low vapor pressure³⁸. In fact, several ILs have been proven to be biocompatible, namely cholinium-based ILs (Cho-ILs), which make them highly attractive for TE applications^{39, 40}.

Despite promising, there are still just few studies reporting the development and application of polymer-based ILs in TE. In addition to this, studies are mostly devoted to muscle regeneration. Ionic electroactive electrospun fibers have been developed based on 1-ethyl-3-methylimidazolium bis(trifluoromethylsulfonyl)imide ([C₂mim][NTf₂]) and PVDF³⁷, showing that [C₂mim][NTf₂] induces the β -phase crystallization of the PVDF fibers, and that the [C₂mim][NTf₂]/PVDF composite fibers show improved cell viability without influencing the morphology of C2C12 cells³⁷. Similar results have been obtained for (1-butyl-3-methylimidazolium chloride [Bmim][Cl] and 2-hydroxyethyl-trimethylammonium dihydrogen phosphate [Ch][DHP]) incorporated into PVDF³⁶.

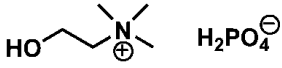
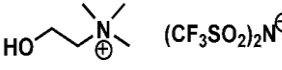
To the best of our knowledge, there is no work reporting on the development and application of polymer-based ILs composites for cardiac TE. In this work, P(VDF-TrFE)/[Ch][DHP] and P(VDF-TrFE)/choline bis(trifluoromethylsulfonyl)imide ([Ch][TFSI]) composite films comprising various IL contents (5, 10 and 20% wt.) were processed solvent casting, characterized and their potential use as scaffolds for cardiac TE applications evaluated. [Ch][DHP] was selected due to its biocompatibility³⁶, whereas [Ch][TFSI] was chosen for its good ionic conductivity (0.398 S.m⁻¹), although [Ch][TFSI] may be toxic when present at high concentrations⁴¹.

2. Experimental section

2.1. Materials

Poly(vinylidene fluoride-co-trifluoroethylene), P(VDF-TrFE), (70:30) was purchased from Solvay. N,N-dimethylformamide (DMF) was obtained from Honeywell and both ILs [Ch][DHP] (purity > 98%) and [Ch][TFSI] (purity > 99%) were acquired from Iolitec. Table 1 shows the chemical structures and the most relevant properties of the ILs used in this work.

Table 1 – Chemical structure, molecular weight, melting temperature and ionic conductivity of the ILs used in this work. Data obtained from the provider.

Ionic Liquid	Chemical structure	Molecular weight (g.mol ⁻¹)	Melting temperature (T _m) (°C)	Ionic conductivity (S.m ⁻¹) (45 °C)
[Ch][DHP]		201.16	190	≤ 0.04
[Ch][TFSI]		368.32	35 – 37	0.398

2.2. Processing of the IL/P(VDF-TrFE) composite films

P(VDF-TrFE) and IL/P(VDF-TrFE) films were processed according to ³². To obtain pristine P(VDF-TrFE) films, P(VDF-TrFE) was dissolved in DMF (20/80 wt.% ratio) under magnetic stirring at room temperature until complete dissolution of the polymer. Then, the polymer solution was poured onto a clean glass substrate and spread over it with a blade. The glass substrate containing the P(VDF-TrFE) solution was placed in an oven (P-Selecta) at 210 °C for 10 min to evaporate the DMF solvent and let to cool down to room temperature. A similar procedure was used for the processing of the IL/P(VDF-TrFE) composites. Different contents of [Ch][DHP] and [Ch][TFSI] (5, 10 and 20% wt.) were first dispersed in DMF and then P(VDF-TrFE) was added to the IL/DMF solution, in a polymer concentration of 20% w/w with respect to the DMF solvent. After the complete P(VDF-TrFE) dissolution, the solution was spread on a glass substrate and placed in an oven at 210 °C for 10 min before letting cool down to room temperature. Thin films with a thickness ranging between 33 and 45 μm were obtained.

2.3. Characterization of the samples

The morphology of the films was analysed by SEM using a NanoSEM-Fei Nova 200 microscope with an acceleration voltage of 10 kV. The samples were previously coated (Polaron SC502 setup) with a thin layer of gold prior to the analysis.

A CSI Nano-Observer AFM microscope with AppNano ANSCM-PT tips was used to analyse the surface roughness and topography of the films. The obtained data were further analysed using the Gwyddion software. The values of the surface roughness for the samples were calculated after measurements at five different zones of the samples (one at each corner of the image and one in the centre) and calculating the value as the average with standard deviation.

The surface wettability of the materials was determined by measuring the contact angle of 3 μL of culture medium at room temperature, using a goniometer (Dataphysics Contact Angle System OCA20). The contact angle of each sample was calculated and presented as the average and standard deviation of six measurements performed at different sample locations. The statistical analysis was performed and all quantitative data were analysed using GraphPad by Dotmatics. The results were analysed statistically using the t-test. Differences were considered to be statistically significant when * $p < 0.05$ and ** $p < 0.01$.

A Bruker Alpha II FTIR spectrometer with a diamond attenuated total internal reflectance (ATR) accessory was used to perform the Fourier Transformed Infrared measurements (FTIR-ATR). The FTIR-ATR spectra of the composites were acquired at room temperature from 4000 to 400 cm^{-1} and collected after 64 scans with a spectral resolution of 4 cm^{-1} .

Differential scanning calorimetry (DSC) measurements were carried out to evaluate the thermal properties of the films. Measurements were performed using a PerkinElmer DSC 6000 instrument under a nitrogen atmosphere. Approximately 5 mg from each sample were placed and sealed into 50 μL aluminium pans and heated from 30 to 200 $^{\circ}\text{C}$ at a heating rate of 10 $^{\circ}\text{C}\cdot\text{min}^{-1}$. The degree of crystallinity (ΔX_c) of each sample was determined from the melting DSC thermograms and applying Equation 1³⁸:

$$\Delta X_c = \frac{\Delta H}{m_{\text{polymer}} \Delta H_{100}} \quad (1)$$

where ΔH is the melting enthalpy of the sample, ΔH_{100} (103.4 J.g^{-1}) is the melting enthalpy for a 100% crystalline sample and m_{polymer} is the mass fraction of polymer within the samples.

Surface (σ_{surface}) and volume (σ_{volume}) electrical conductivity of the samples were evaluated from the current (I) - voltage (V) curves measured at room temperature with a Keithley 6487 picoammeter/voltage source applying voltages from -10 to 10 V. The samples were coated by magnetron sputtering with gold electrodes using a SC502 sputter coater. For the surface electrical conductivity measurements, two parallel rectangular (3 x 6 mm) gold electrodes were deposited side by side (1 mm apart) on one side of the sample while for the volume electrical conductivity measurements, two gold electrodes with 5 mm diameter were deposited onto both sides of the sample. The (σ_{surface}) and (σ_{volume}) electrical conductivity were calculated by applying Equation 2⁴² and Equation 3⁴³, respectively:

$$\sigma_{\text{surface}} = \frac{1}{R \frac{L}{D}} \quad (2)$$

where R is the surface resistance, D is the length of the electrode (3 mm) and L is the distance between the electrodes (1 mm).

$$\sigma_{\text{volume}} = \frac{1}{RA/L} \quad (3)$$

where R is the electrical resistance, L is the sample thickness and A is the area of the electrodes.

2.4. Cell culture

H9c2 myoblast cells (a rat heart myoblast cell line routinely used as an experimental model) were grown in a 75 cm^2 cell culture flask using in Dulbecco's Modified Eagle's Medium (DMEM, Sigma Aldrich) containing 4.5 g.L^{-1} glucose, 10% Fetal Bovine Serum (FBS, Biochrom) and 1% Penicilin/Streptomycin (P/S, Biochrom) in a $37 \text{ }^\circ\text{C}$ incubator under 95% humidified air and 5% CO_2 . The culture medium was changed every two days and when H9c2 cells reached approximately 70% confluence, they were trypsinized with 0.05% trypsin-EDTA (Biochrom, Berlin, Germany).

2.5. Cell toxicity assays

Indirect cell toxicity assays were performed with H9c2 cells. For that purpose, the 3-(4,5-dimethylthiazol-2-yl)-5-(3-carboxymethoxyphenyl)-2-(4-sulfophenyl)-2H-tetrazolium (MTS, Promega) assay was used for assessing the metabolic activity of the cells. Before beginning the *in vitro* assays, the samples were sterilized. In this way, circular samples from P(VDF-TrFE) and IL/P(VDF-TrFE) films were cut with 13 mm of diameter and exposed to ultraviolet light (UV) for 1 h each side. Thereafter, the samples were washed 4 times with sterile phosphate-buffered saline solution (PBS, pH 7.4) for 5 min and placed in a 24-well tissue culture polystyrene plate. Following sterilization, the samples were placed in a 24-well tissue culture polystyrene plate and exposed for 72 h to culture medium at 37 °C in 95% humidified air containing 5% CO₂. Two days later, H9c2 cells were seeded in a 96-well tissue culture plate at 3 x 10⁴ cells·mL⁻¹ for 24 h to allow cell attachment. Then, the H9c2 culture medium was discarded and replaced by the culture medium that was in contact (for 72 h) with the different samples. In this experiment, it was also used a negative control (DMEM) and a positive control (dimethylsulfoxide (DMSO) at 20%). The cells were then incubated for 72 h and their metabolic activity was quantified by an MTS assay, replacing the medium of each well with fresh medium containing MTS solution (dilution of 1:5 in DMEM). The absorbance was measured using a microplate reader (Biotech Synergy HT) at 490 nm after 2 h of incubation in the dark at 37 °C. Four replicate absorbance measurements were performed. The cell viability was calculated according to equation 4:

$$\text{Cell viability (\%)} = \frac{\text{absorbance of sample}}{\text{negative control absorbance}} \times 100 \quad (4)$$

2.6. Cell proliferation assays

Circular samples from P(VDF-TrFE) and IL/P(VDF-TrFE) films were cut with 11 mm of diameter, sterilized as described above and placed in a 48-well tissue culture polystyrene plate. Afterwards, H9c2 cell suspension was seeded on the top of each film by the drop method (80 µL of DMEM containing 7000 cells (cell density = 8.75 x 10⁴ cells·mL⁻¹)). This method was used to ensure that cells adhere to the surface of the material and not to the plate. After 24 and 72 h of incubation, the samples were transferred to a new 48-well plate and incubated with medium containing MTS solution (dilution of 1:5 in DMEM). After 2 h of incubation in the dark at 37 °C and 5% CO₂, 100 µL of each well was

transferred in triplicate to a 96-well plate and the absorbance was measured at 490 nm using a microplate reader (Biotech Synergy HT).

2.7. Immunofluorescence staining

Immunofluorescence staining was performed in order to evaluate the adhesion of H9c2 cells to the IL/P(VDF-TrFE) composites 24 h after the beginning of the cell proliferation assay under static conditions. For that, it was used 4',6-diamidino-2-phenylindole (DAPI, Sigma Aldrich) to stain the H9c2 myoblast nucleus and tetramethylrhodamine B isothiocyanate (TRITC, Sigma Aldrich) to stain the actin cytoskeleton of the cells. After 24 h of incubation, the cell culture medium was removed carefully and the samples were washed three times with PBS solution for 5 min. H9c2 cells were then fixated with 4% paraformaldehyde (Panreac) for 10 min at 37 °C, washed three times with PBS solution for 5 min, and permeabilized with 0.1% Triton X-100 for 10 min at room temperature. After this, the cells were subsequently washed twice with PBS for 5 min and stained with TRITC ($0.1 \mu\text{g}\cdot\text{mL}^{-1}$) in the dark at room temperature for 45 min. After washing twice with PBS solution, the cells were then stained with DAPI ($1 \mu\text{g}\cdot\text{mL}^{-1}$) in the dark at room temperature for 5 min. Finally, the samples were washed twice with PBS solution, followed by one 5 min wash in distilled water. An Olympus BX51 fluorescence microscope was used to visualize the samples.

3. Results and discussion

3.1 Morphological features and surface contact angle

The cross-section morphology of the IL/P(VDF-TrFE) composites was evaluated by SEM and representative images are shown in Figure 1 for composites with different IL contents. Pristine P(VDF-TrFE) films (Figure 1a) presents a compact morphology without pores, which is in agreement with previous studies⁴⁴. When P(VDF-TrFE) is processed after solvent evaporation at high temperatures (210 °C), the polymer chains have enough mobility to occupy the empty spaces left by the evaporated solvent, resulting in a more compact structure⁴⁵. Further, this compact structure is not significantly altered after the incorporation of [Ch][DHP] and [Ch][TFSI] within the polymer matrix (Figure 1b-g).

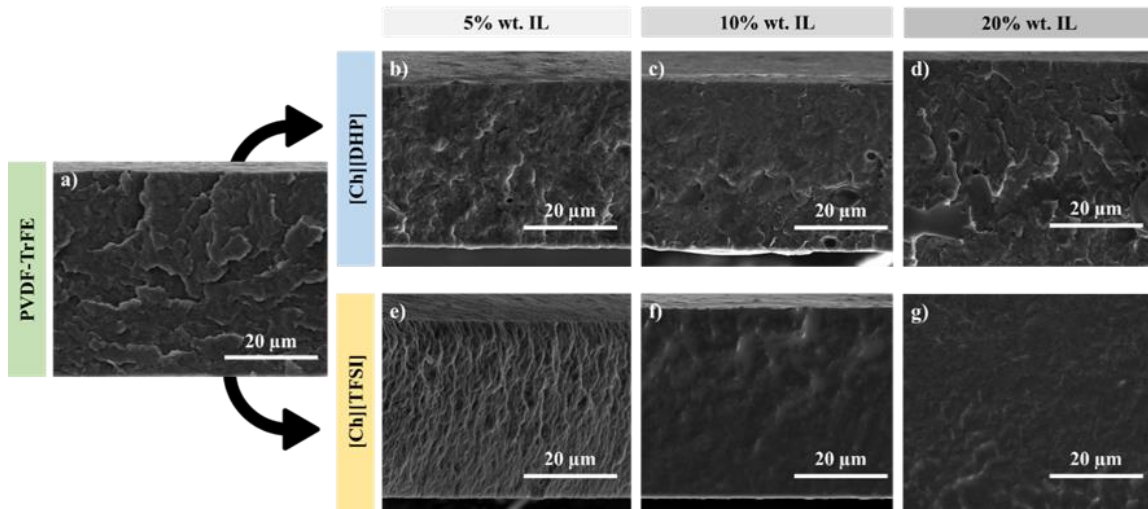


Figure 1 – Cross section SEM images of: a) pristine P(VDF-TrFE) and IL/P(VDF-TrFE) composite films with b) 5, c) 10 and d) 20% wt. of [Ch][DHP] and e) 5, f) 10 and g) 20% wt. of [Ch][TFSI], respectively.

The surface topography and roughness of the samples was evaluated by AFM microscopy. Figure 2 shows representative topography surface of the different samples and Table 2 presents the corresponding surface mean roughness (R_a) values.

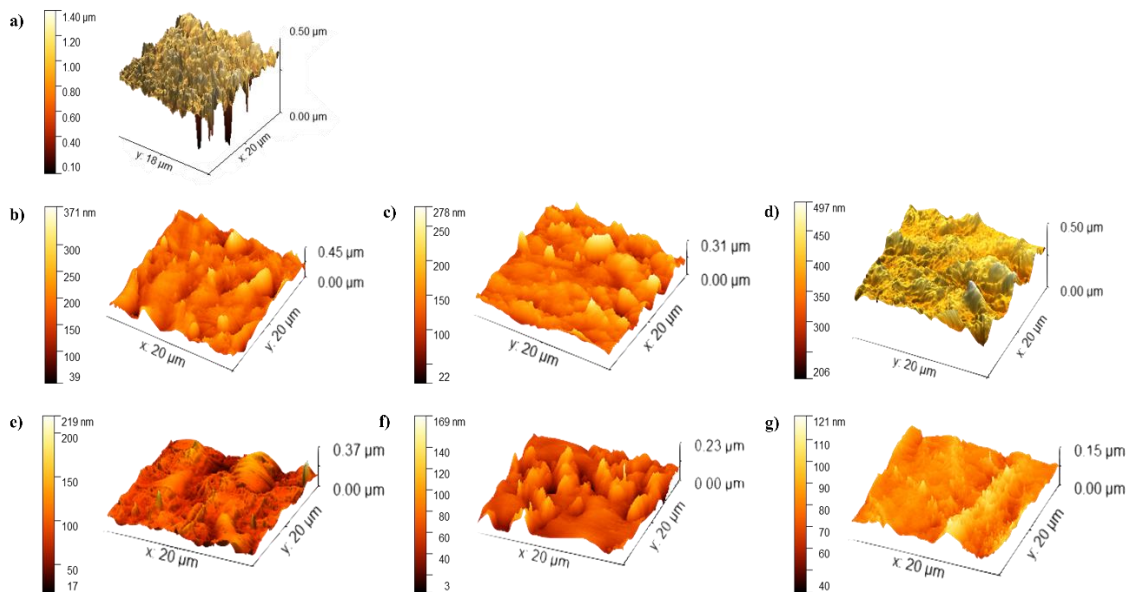


Figure 2 – AFM images of: a) pristine P(VDF-TrFE) and IL/P(VDF-TrFE) composite films with b) 5, c) 10 and d) 20% wt. of [Ch][DHP] and e) 5, f) 10 and g) 20% wt. of [Ch][TFSI], respectively.

Regardless of the IL within the composite, its incorporation into the polymer matrix induces important variations in the surface topography as well on the surface roughness of the films. The surface of P(VDF-TrFE) films (Figure 2a) is considerably rougher and less homogeneous than for the [Ch][DHP]/P(VDF-TrFE) (Figure 2c-d) and

[Ch][TFSI]/P(VDF-TrFE) composites films (Figure 2e-g). Apart from it, it is verified that the surface mean roughness (R_a) of the pristine copolymer (71 ± 15 nm) strongly decreases with the incorporation of both ILs and also decreases with increasing IL content, being the latter more accentuated for [Ch][TFSI], which is related to the higher molecular weight of this IL (Table 1) and corresponding higher ion-dipole interaction area with the polar polymer chains ⁴⁶.

Table 2 – Average surface roughness (R_a) values of pristine P(VDF-TrFE) and IL/P(VDF-TrFE) composite films, as obtained from the AFM measurements.

Sample	% IL content	R_a (nm)
P(VDF-TrFE)	0	71 ± 15
	5	32 ± 14
[Ch][DHP]/P(VDF-TrFE)	10	21 ± 4
	20	23 ± 3
	5	23 ± 3
[Ch][TFSI]/P(VDF-TrFE)	10	15 ± 4
	20	8 ± 2

The variation of the surface roughness, together with variations in the surface chemistry, typically leads to variations in the surface wettability of the samples ⁴⁷, which has been assessed through the sessile drop technique by measuring the contact angle of a culture medium droplet placed on the surface of the films ⁴⁸. The surface of a material is considered hydrophilic when the contact angle value is below 90° and hydrophobic when it is above 90° ^{49, 50}. The results for the different samples are presented in Figure 3, showing that the developed films are hydrophilic. Further, the surface wettability of P(VDF-TrFE) is affected by the incorporation of both [Ch][DHP] and [Ch][TFSI], as a consequence of the hygroscopic nature of the ILs and IL-polymer interactions which, together with the surface chemistry modifications by the presence of IL in the surface, also decreases the interactions between cation-anion in the IL, and consequently, leads to higher surface tension of the composites ^{36, 51}. Further, the contact angle values decrease with increasing IL content within the composites. With respect to the effects of each IL, for the composite films based on [Ch][DHP], its incorporation leads to a slight decrease in the contact angle values, from about $85 \pm 3^\circ$ for pristine P(VDF-TrFE) to $76 \pm 2.5^\circ$ for

10% wt. [Ch][DHP] composites. The surface contact angle of the composite films containing 20% wt. [Ch][DHP] content cannot be determined since the droplet was totally absorbed by the film after 60 seconds, displaying a superhydrophilic behaviour. In the case of [Ch][TFSI] composites, the incorporation of [Ch][TFSI] leads to a decrease in the contact angle values down to 77 to $61 \pm 2^\circ$ for the 20%wt. loaded composite. The difference between the surface wettability of the [Ch][DHP] and [Ch][TFSI] composites is mainly ascribed to the hygroscopic nature of the ILs. The surface contact angle of P(VDF-TrFE) slightly decreases with the incorporation of both IL and also decreases with increasing IL content, being the latter more accentuated for [Ch][DHP], which is related to the higher affinity of this IL for water^{52, 53}.

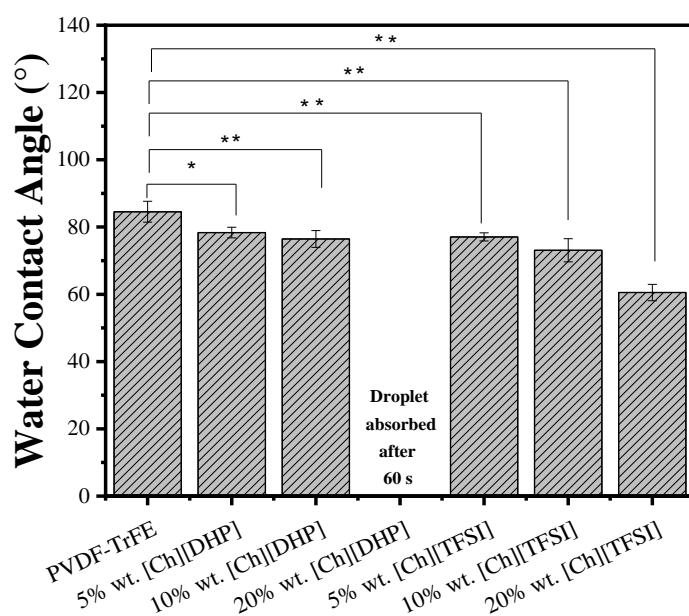


Figure 3 – Contact angles for P(VDF-TrFE), [Ch][DHP]/P(VDF-TrFE) and [Ch][TFSI]/P(VDF-TrFE) composite films comprising various IL contents (5, 10 and 20% wt.). * $p < 0.05$, ** $p < 0.01$.

3.2 Vibrational spectra, thermal and electrical properties

FTIR-ATR measurements were performed to evaluate the influence of the inclusion of the ILs on the polymer matrix. The FTIR-ATR spectra of the P(VDF-TrFE) and IL/P(VDF-TrFE) composite films with 5, 10 and 20% wt. IL content are presented in Figure 4a-b and their main FTIR absorption bands are presented in Table S1 in the supplementary information. The presence of the main absorption bands characteristics of the polar β -phase of PVDF (842 and 1289 cm^{-1}) and the absence of the characteristic

bands of the α - and γ -phase of the polymer in the films, indicates that, independently of IL type and content, P(VDF-TrFE) crystallizes mainly in the electroactive β -phase, in agreement to related studies^{54,55}. Other absorption bands assigned to the β -phase of the polymer are detected: 465, 502, 882 and 1171 cm^{-1} (CF_2 stretching vibration), 1400 cm^{-1} (C-C symmetric stretching vibration) and 1432 cm^{-1} (bending and wagging vibrational modes of CH_2)³¹. For [Ch][DHP]/P(VDF-TrFE) composite films (Figure 4a), the absorption bands detected at 950, 1479 and 1644 cm^{-1} are attributed to C-N stretching of the [Chol]⁺ cation, CH_3 rocking and O-H vibration, respectively^{36,56,57}. In the case of [Ch][TFSI]/P(VDF-TrFE) films (Figure 4b), the absorption bands at 612, 740, 790, and 1132 are related to the [TFSI]⁻ anion^{58,59}. While the band detected at 612 cm^{-1} corresponds to the antisymmetric bending of SO_2 molecule in the [TFSI]⁻ anion⁵⁸, the bands observed at 740, 790 and 1132 cm^{-1} are assigned to the cis [TFSI]⁻ conformation^{58,59}, stretching vibration of C-S molecule in the [TFSI]⁻ anion⁵⁷ and symmetric stretching vibration of SO_2 molecule in [TFSI]⁻ anion⁵⁸, respectively. Other characteristics absorption bands of [Ch][TFSI] are found at 953 cm^{-1} (rocking vibration of CH_3 molecule in [Chol]⁺ cation)^{57,60}, 1051 cm^{-1} (S-N-S asymmetrical stretching in [TFSI]⁻ cation)⁵⁸, 1349 cm^{-1} (symmetric stretching vibration of the SO_2 group of the [TFSI]⁻ anion)⁵⁸ and 1479 cm^{-1} (C-H bending of the methyl group in [TFSI]⁻ anion)⁵⁸. No new bands are observed in the FTIR-ATR spectra of the [Ch][DHP]/P(VDF-TrFE) and [Ch][TFSI]/P(VDF-TrFE) composite films, compatible with electrostatic nature of the interactions between the anions and cations of the IL and highly polar polymer chains of the matrix^{36,54}.

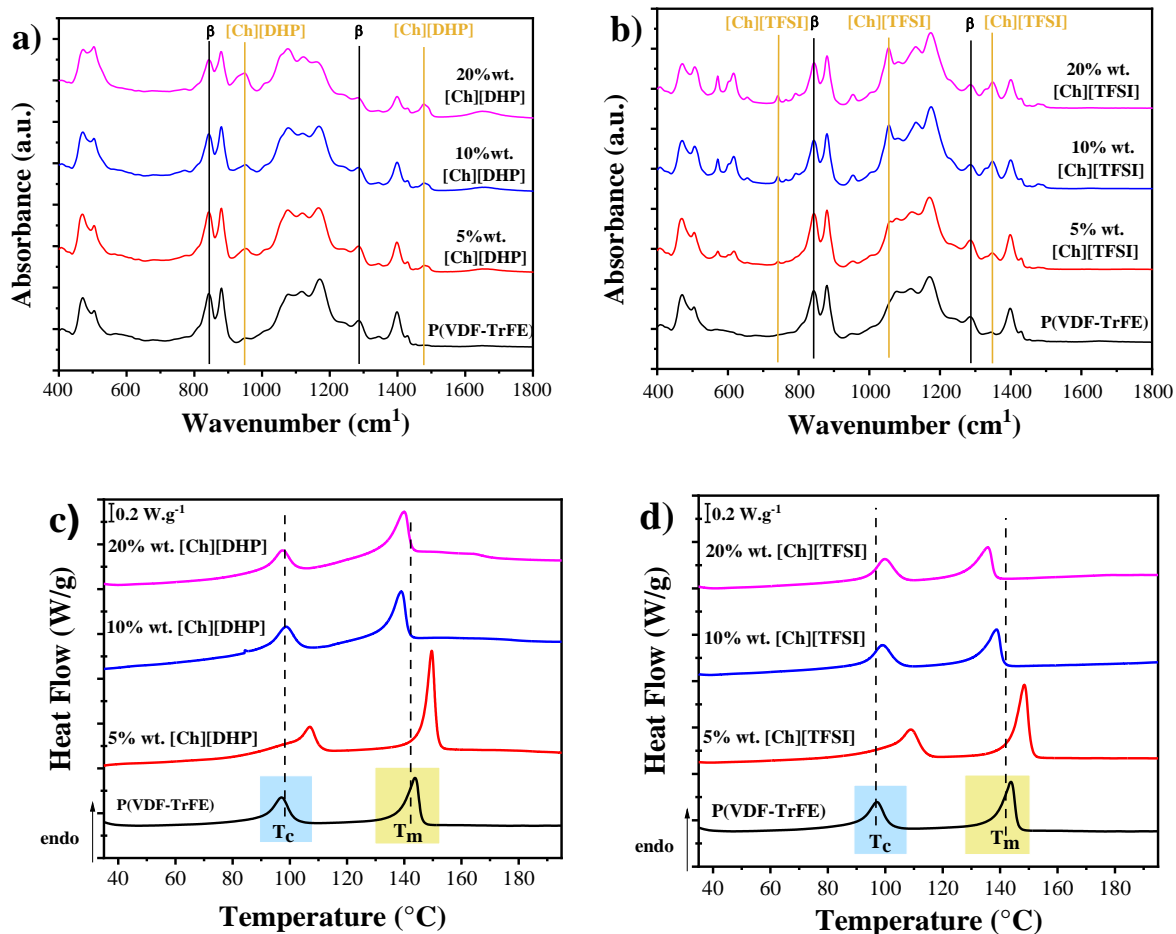


Figure 4 – FTIR-ATR spectra for pristine P(VDF-TrFE) and a) [Ch][DHP]/P(VDF-TrFE) and b) [Ch][TFSI]/P(VDF-TrFE) composite films incorporating different IL contents (5, 10 and 20 % wt.). DSC thermograms for pristine P(VDF-TrFE) and c) [Ch][DHP]/P(VDF-TrFE) and d) [Ch][TFSI]/P(VDF-TrFE) composite films with 5, 10 and 20% wt. IL content.

DSC was carried out to evaluate the influence of the IL type and content in the thermal properties of the composites. The DSC thermograms of pristine P(VDF-TrFE) and the IL/P(VDF-TrFE) composite films containing different IL contents are presented in Figure 4c-d. The thermograms of both pristine P(VDF-TrFE) and IL/P(VDF-TrFE) composites are characterized by the two endothermic peaks found in P(VDF-TrFE). The first endothermic peak is observed between 97 and 109 °C and corresponds to the ferroelectric to paraelectric transition (Curie temperature (T_c)) and the higher temperature one that appears between 135 and 150 °C refers to the melting temperature (T_m) of the polymer^{31, 61}. Further, the incorporation of 5% wt. of [Ch][DHP] and [Ch][TFSI] shift both T_c and T_m temperatures to higher temperatures, indicative a stabilization of both ferroelectric and crystalline phases though the electrostatic ion-dipole interactions with respect to the

pristine polymer ⁶². This behaviour is not observed upon the incorporation of 10 and 20% wt. of [Ch][DHP] and [Ch][TFSI] into the P(VDF-TrFE) polymer matrix, the transition temperatures remaining similar to the pristine polymer or even slightly decreasing, which is attributed to increased IL-IL interactions for higher IL concentrations, that effectively diminished the effectiveness of the ion-dipole interactions ⁶³.

The crystallinity degree (ΔX_c) of the composites was calculated applying the equation 1 and the results are presented in Table 3. Independently of the IL type, the incorporation of 5% wt. IL leads to an increase in the crystallinity degree in comparison with pristine P(VDF-TrFE), demonstrating that, at this concentration, both ILs act as a nucleating agent during the crystallization process of the polymer ⁵⁴. Nonetheless, a different behaviour is observed for higher IL concentrations. In the case of composites with [Ch][DHP], the incorporation of 10 and 20% wt. of IL does not affect the crystallization process of the P(VDF-TrFE) polymer since no significant differences are observed in the crystallinity degree of [Ch][DHP]/P(VDF-TrFE) composites. Concerning composites with [Ch][TFSI], the degree of crystallinity decreases with increasing IL content from 26 to 17%, indicating that for higher IL contents, [Ch][TFSI] act as defect during the P(VDF-TrFE) crystallization process ⁵⁴. As previously mentioned, this effect is related to the increased IL-IL interactions for higher IL concentrations, that screens the ion-dipole interactions dominant for lower IL concentrations ⁶².

Table 3 – Curie temperature (T_c), melting temperature (T_m) and degree of crystallinity of pristine P(VDF-TrFE) and IL/P(VDF-TrFE) composite films. The associated error is $\pm 2\%$

Sample	% IL content	T_c	T_m	ΔX_c
P(VDF-TrFE)	0	97	144	17
[Ch][DHP]/P(VDF-TrFE)	5	107	150	25
	10	98	141	22
	20	96	141	26
[Ch][TFSI]/P(VDF-TrFE)	5	109	148	26
	10	99	139	15
	20	100	136	17

As the samples are intended for being used as active scaffolds for biomedical applications, together with the measurements of the electrical conductivity, the influence of the

sterilization process on the surface (σ_{surface}) and volume (σ_{volume}) electrical conductivity of the IL/P(VDF-TrFE) composites has been addressed. For that, the samples were submitted to two treatments: (i) exposed to UV for 1 h each side – (UVs); and (ii) washed 4 times with PBS solution for 5 minutes – (PBS washing). The untreated samples were used as control group. Figure 5 shows the σ_{surface} and σ_{volume} of untreated and treated P(VDF-TrFE) and IL/P(VDF-TrFE) composite films. Figure 5 shows that, previous to the sterilization process, the introduction of the ILs in the P(VDF-TrFE) leads to an increase of both σ_{surface} and σ_{volume} of the composites when compared to pristine P(VDF-TrFE) ($\sigma_{\text{surface}} = 8.33 \times 10^{-13} \text{ S.m}^{-1}$ and $\sigma_{\text{volume}} = 4.22 \times 10^{-12} \text{ S.m}^{-1}$), being the increase of several orders of magnitude for filler contents above 10% wt. The surface conductivity of the IL/P(VDF-TrFE) composites increases with increasing IL from 1×10^{-12} for 5% wt. [Ch][DHP] to $5 \times 10^{-9} \text{ S.m}^{-1}$ in the composites with 20% wt. [Ch][DHP] (Figure 5a) and from about 2.5×10^{-8} for 5% wt. [Ch][TFSI] to $1.5 \times 10^{-7} \text{ S.m}^{-1}$ for 20% wt. [Ch][TFSI] composites (Figure 5b). The σ_{volume} , also increases with increasing IL content from 1.8×10^{-8} for 5% wt. [Ch][DHP] to $1.17 \times 10^{-5} \text{ S.m}^{-1}$ in the composites with 20% wt. [Ch][DHP] (Figure 5c) and from 2.3×10^{-6} for 5% wt. [Ch][TFSI] to $1.14 \times 10^{-4} \text{ S.m}^{-1}$ for 20% wt. [Ch][TFSI] composites (Figure 5d).

Concerning the influence of UV sterilization on the σ_{surface} and σ_{volume} of the composites, no significant differences are observed in either case. Contrarily, PBS washing strongly influences the σ_{surface} of the composites, decreasing to lower values in both IL/P(VDF-TrFE) composites, but more pronounced in the [Ch][DHP] composites. In the case of σ_{volume} , no significant differences are observed. Thus, it is confirmed that some of the IL remains in the surface of the polymer composites that is removed by PBS washing.

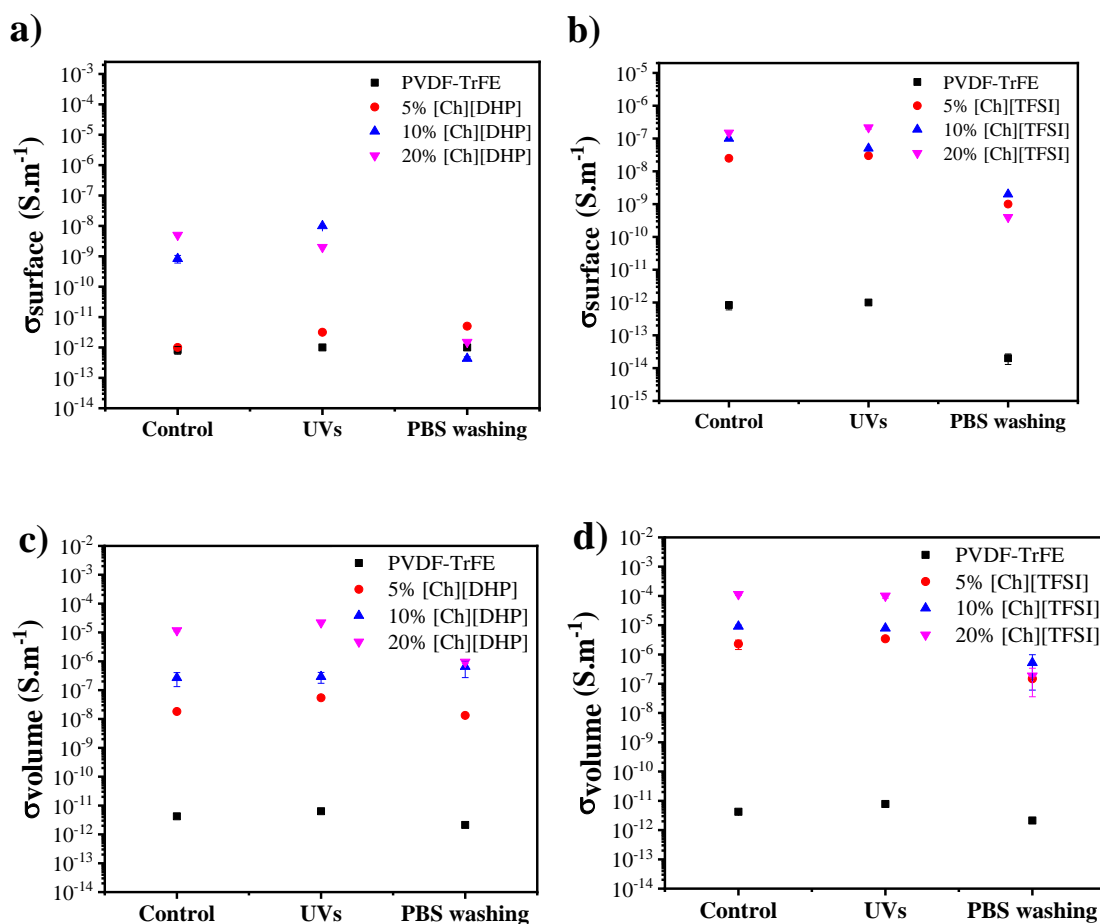


Figure 5 – Surface (a and b) and volume (c and d) electrical conductivity of P(VDF-TrFE) and IL/P(VDF-TrFE) composite films comprising different IL contents (5, 10 and 20% wt.).

3.3 Cytotoxicity and cell viability

There are several requirements that must be taken into consideration during the development of scaffolds for tissue regeneration, being non-cytotoxicity and biocompatibility two of them. In this way, the cytotoxic effect of the IL/P(VDF-TrFE) composite films was analysed with H9c2 cells, a rat embryonic cell line. The results are presented in Figure 6a. According to the ISO standard 10993-5, a sample is considered cytotoxic when cell viability values are below 70%⁶⁴. Thereby, it can be concluded that only the [Ch][DHP]/P(VDF-TrFE) composites are not cytotoxic to H9c2 cells since the composites with [Ch][TFSI] present a viability value below 70% (Figure 6a). The cytotoxicity observed for the [Ch][TFSI]/P(VDF-TrFE) composites may be attributed to an increase in acidity of the medium, due to the toxicity associated to the [TFSI]⁻ anion⁵¹. From cell viability results, it is also possible to verify that [Ch][DHP] content

influences the cell viability. Thus, only the [Ch][DHP]/P(VDF-TrFE) composites will be used for cell proliferation assays in direct contact experiments.

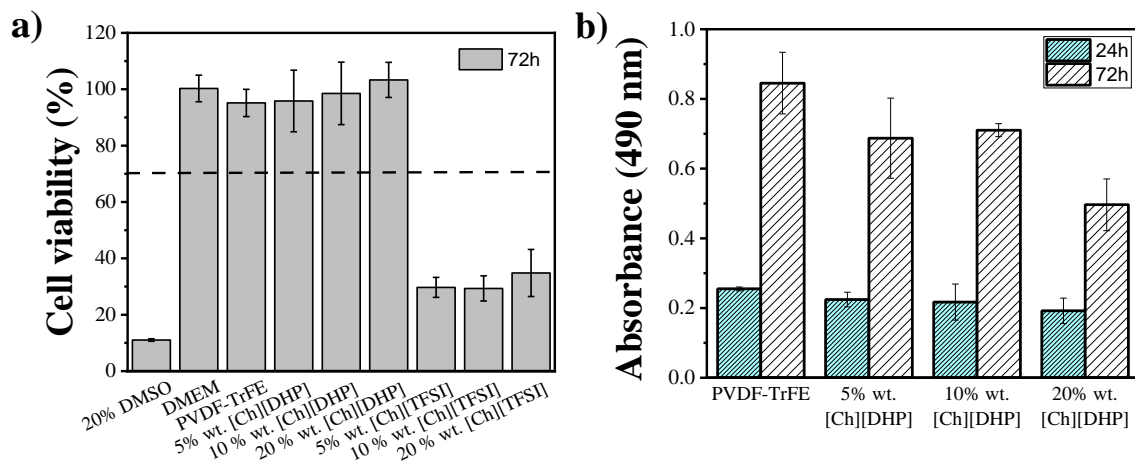


Figure 6 – a) Cytotoxicity assays for H9c2 cells in contact with the as-prepared extraction media exposed to the IL/P(VDF-TrFE) composites with different [Ch][DHP] and [Ch][TFSI] contents for 72 h (relative cell viability was presented as the percentage of the negative control (DMEM, $n = 4 \pm SD$). b) MTS assay results from static proliferation assay of H9c2 cells seeded on different [Ch][DHP]/P(VDF-TrFE) composite films after 24 and 72 h. Results are expressed as mean \pm standard deviation with $n = 3$.

Following cell toxicity assays, the cell viability of H9c2 cells growing on different [Ch][DHP]/P(VDF-TrFE) composites films was assessed using MTS assay and the obtained results are presented in Figure 6b. The H9c2 cell viability increases in all the samples from 24 to 72 h, presenting the P(VDF-TrFE) pristine films the highest cell viability value for both timepoints. Further, it is also observed that [Ch][DHP] content influences the viability of H9c2 myoblast cells. Although no significant differences were observed in cell viability of the composite films after 24 h of cell culture, the H9c2 cell viability decreases after 72 h with increasing IL content, from 0.69 to 0.50. It is well established that the surface wettability, the degree of crystallinity as well as the surface roughness, are parameters which strongly affect the cell-biomaterial interaction and, consequently, cell adhesion, proliferation, and differentiation. As the degree of the crystallinity of the composites is quite similar, the decrease in the viability of the H9c2 myoblast cells may be due to the surface wettability of the [Ch][DHP] composites. According to the literature, cells spread more on hydrophilic surfaces, particularly on those with a moderate contact angle, between 70 and 80°, which explains the obtained results⁶⁵. The surface wettability of the [Ch][DHP] composites increase with the

increasing IL, presenting the composites with 20% wt. [Ch][DHP] a superhydrophilic behaviour and, consequently, the lowest cell viability value for 72 h. Concerning surface roughness, it has been reported that samples with higher roughness show improved attachment and proliferation of H9c2 cells [65]. Observing AFM results, the surface topography of P(VDF-TrFE) films is considerably rougher than that of the [Ch][DHP]/P(VDF-TrFE) composites, which explains the obtained cell viability results and demonstrates that the surface roughness of the given materials affects the cell-biomaterial interaction and, consequently, cell adhesion and proliferation. Furthermore, the electrical conductivity can also affect the cell behaviour⁶⁶. Relatively to the surface electrical conductivity, similar values were obtained for all the samples after the PBS washing but it is verified that the volume electrical conductivity is higher for the composites of 10% and 20% wt. with no significant differences among both. Nevertheless, the obtained values (Figure 6b) show that the composites with 10% wt. present higher values, which can lead to conclude that the electrical conductivity may play a relevant role too.

Immunofluorescence staining was performed with the aim of evaluating the adhesion of H9c2 cells to the IL/P(VDF-TrFE) composites after 24 h under static conditions. Immunofluorescence images (Figure 7) show that H9c2 cells adhered well both to pristine P(VDF-TrFE) and [Ch][DHP] composite films, showing less cells adhered on the samples with 20% [Ch][DHP], which is in agreement with the MTS results obtained (Figure 6b). Regarding the cell morphology, no significant differences are observed on the different composites.

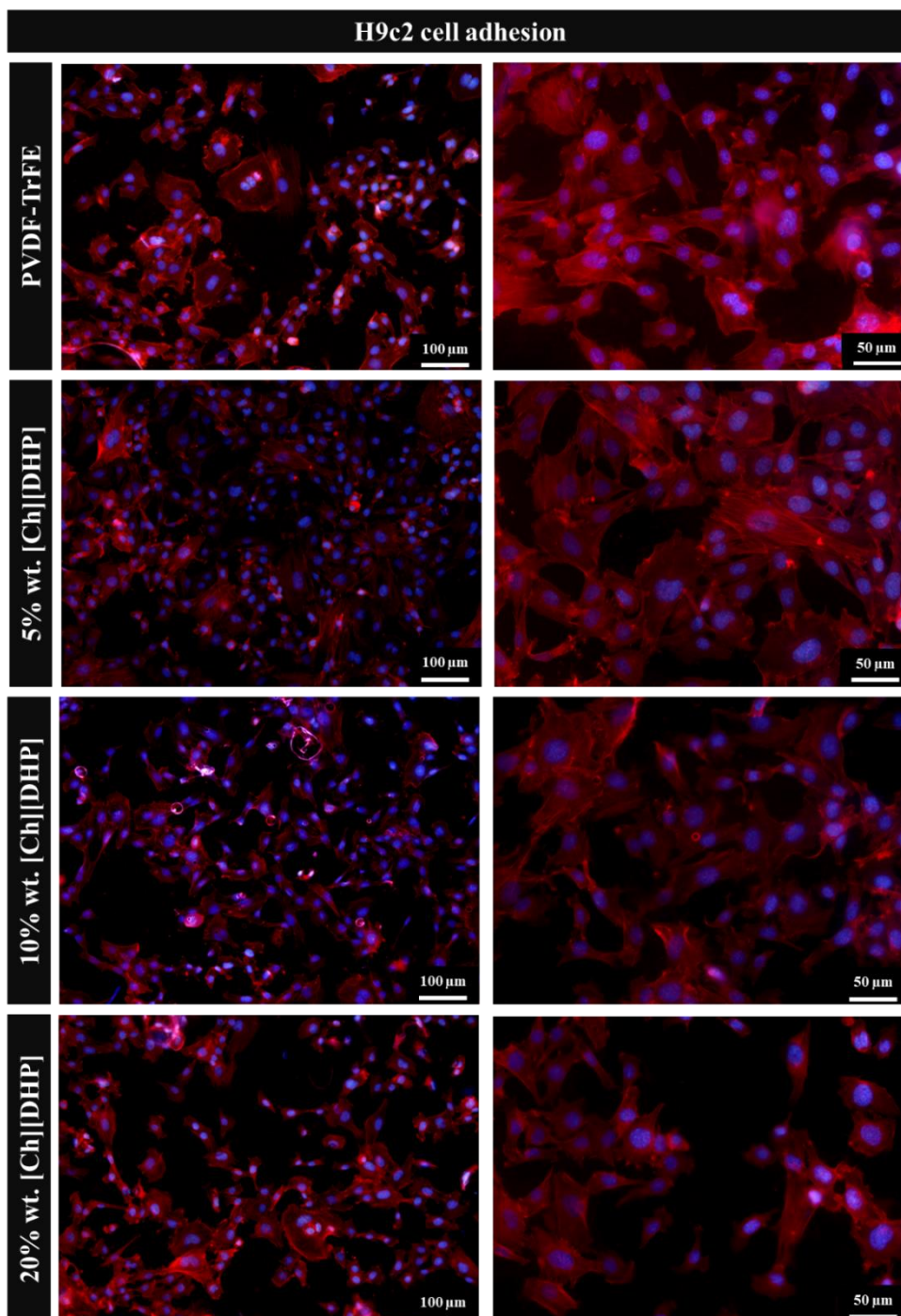


Figure 7 – Cell adhesion of H9c2 cells on pristine P(VDF-TrFE) and on [Ch][DHP]/P(VDF-TrFE) composite films comprising various [Ch][DHP] contents (5, 10 and 20% wt.).

Conclusions

Ionic electroactive materials based on P(VDF-TrFE) and two different ILs, [Ch][DHP] and [Ch][TFSI], comprising different contents (5, 10 and 20% wt.) were successfully prepared by a solvent casting method.

The incorporation of both IL maintains the compact morphology of the processed films, which is similar to the one of the pristine polymer. The incorporation of the ILs induces changes in the surface topography and surface roughness of the composites from 71 ± 15 nm for the pristine polymer to 23 ± 3 for the 20% wt. [Ch][DHP] composites, and to 8 ± 2 for the 20% wt. [Ch][TFSI] composites, as well as on the surface wettability and on the electrical properties of the IL/P(VDF-TrFE) composites, increasing surface wettability and σ_{surface} and σ_{volume} of the composites with the increasing IL content, reaching maximum values of $61 \pm 2^\circ$, $1.5 \times 10^{-7} \text{ S.m}^{-1}$ and $1.14 \times 10^{-4} \text{ S.m}^{-1}$, respectively, for the [Ch][TFSI]/P(VDF-TrFE) composites.

It is also concluded that the sterilization process strongly affects the electrical conductivity of some of the composites. In particular, PBS washing strongly decreases the conductivity of both composites, whereas σ_{surface} and σ_{volume} of the composites remains almost unaltered after UV sterilization.

Regarding the degree of crystallinity of the composites, the incorporation of 5% wt. of IL leads to an increase in the degree of crystallinity, demonstrating that, at this concentration, both ILs act as a nucleating agent during the crystallization process of the polymer. No significant differences were observed in the degree of crystallinity of the [Ch][DHP]/P(VDF-TrFE) composites upon the incorporation of 10 and 20% wt. of IL.

Finally, just the [Ch][DHP]/P(VDF-TrFE) does not show any cytotoxic effect on H9c2 cells, the composites supporting H9c2 myoblast cell adhesion and proliferation, demonstrating their potential use as suitable platform for cardiac tissue regeneration.

Acknowledgments

Work was supported by FCT – Fundação para a Ciência e Tecnologia (FCT): strategic funding UID/FIS/04650/2020 unit, projects PTDC/BTM-MAT/28237/2017, grants SFRH/BD/148655/2019 (R.M.M) and SFRH/BPD/121526/2016 (D.M.C) and contract 2020.04163.CEECIND (C.R). Funding by the Spanish State Research Agency (AEI) and the European Regional Development Fund (ERFD): PID2019-106099RB-C43/AEI/10.13039/501100011033 and the Basque Government Industry Department (ELKARTEK program) and Education Department (grant PRE_2020_1_0201, A.G.D) is acknowledged.

References

1. A. Silvestri, M. Boffito, S. Sartori and G. Ciardelli, *Macromol Biosci*, 2013, **13**, 984-1019.
2. A. Moorthi, Y. C. Tyan and T. W. Chung, *Biomater Sci*, 2017, **5**, 1976-1987.
3. M. Isomi, T. Sadahiro and M. Ieda, *J Cardiol*, 2019, **73**, 97-101.
4. B. Fujita and W. H. Zimmermann, *Interact Cardiovasc Thorac Surg*, 2018, **27**, 916-920.
5. M. Tallawi, E. Rosellini, N. Barbani, M. G. Cascone, R. Rai, G. Saint-Pierre and A. R. Boccaccini, *J R Soc Interface*, 2015, **12**, 20150254.
6. A. Patino-Guerrero, J. Veldhuizen, W. Zhu, R. Q. Migrino and M. Nikkhah, *Journal of Materials Chemistry B*, 2020, **8**, 7571-7590.
7. F. J. O'Brien, *Materials Today*, 2011, **14**, 88-95.
8. C. Ribeiro, D. M. Correia, S. Ribeiro, V. t. Sencadas, G. Botelho and S. Lanceros-Mendez, *Engineering in Life Sciences*, 2015, **15**, 351-356.
9. W. L. Stoppel, D. L. Kaplan and L. D. Black, 3rd, *Adv Drug Deliv Rev*, 2016, **96**, 135-155.
10. N. J. Kaiser and K. L. Coulombe, *Biomed Mater*, 2015, **10**, 034003.
11. J. Leor, S. Tuvia, V. Guetta, F. Manczur, D. Castel, U. Willenz, O. Petnehazy, N. Landa, M. S. Feinberg, E. Konen, O. Goitein, O. Tsur-Gang, M. Shaul, L. Klapper and S. Cohen, *J Am Coll Cardiol*, 2009, **54**, 1014-1023.
12. M. Tamimi, S. Rajabi and M. Pezeshki-Modaress, *Int J Biol Macromol*, 2020, **164**, 389-402.
13. Y. Zhang, D. Zhu, Y. Wei, Y. Wu, W. Cui, L. Liuqin, G. Fan, Q. Yang, Z. Wang, Z. Xu, D. Kong, L. Zeng and Q. Zhao, *Acta Biomater*, 2019, **86**, 223-234.
14. P. Benzoni, P. Ginestra, L. Altomare, A. Fiorentino, L. De Nardo, E. Ceretti and P. Dell'Era, *Procedia CIRP*, 2016, **49**, 113-120.
15. Y. Liu, S. Wang and R. Zhang, *Int J Biol Macromol*, 2017, **103**, 1130-1137.
16. B. Fu, X. Wang, Z. Chen, N. Jiang, Z. Guo, Y. Zhang, S. Zhang, X. Liu and L. Liu, *Journal of Materials Chemistry B*, 2022, **10**, 656-665.
17. N. Wang, C. Liu, X. Wang, T. He, L. Li, X. Liang, L. Wang, L. Song, Y. Wei, Q. Wu and C. Gong, *Theranostics*, 2019, **9**, 1980-1992.
18. R. Gaetani, D. A. Feyen, V. Verhage, R. Slaats, E. Messina, K. L. Christman, A. Giacomello, P. A. Doevendans and J. P. Sluijter, *Biomaterials*, 2015, **61**, 339-348.
19. K. Elkhoury, M. Morsink, L. Sanchez-Gonzalez, C. Kahn, A. Tamayol and E. Arab-Tehrany, *Bioact Mater*, 2021, **6**, 3904-3923.
20. H. Cui, J. Shao, Y. Wang, P. Zhang, X. Chen and Y. Wei, *Biomacromolecules*, 2013, **14**, 1904-1912.
21. B. S. Spearman, A. J. Hodge, J. L. Porter, J. G. Hardy, Z. D. Davis, T. Xu, X. Zhang, C. E. Schmidt, M. C. Hamilton and E. A. Lipke, *Acta Biomater*, 2015, **28**, 109-120.
22. K. Ashtari, H. Nazari, H. Ko, P. Tebon, M. Akhshik, M. Akbari, S. N. Alhosseini, M. Mozafari, B. Mehravi, M. Soleimani, R. Ardehali, M. Ebrahimi Warkiani, S. Ahadian and A. Khademhosseini, *Adv Drug Deliv Rev*, 2019, DOI: 10.1016/j.addr.2019.06.001.
23. A. Gelmi, M. K. Ljunggren, M. Rafat and E. W. H. Jager, *Journal of Materials Chemistry B*, 2014, **2**, 3860-3867.
24. C. Ribeiro, V. Sencadas, D. M. Correia and S. Lanceros-Mendez, *Journal*, 2015, **136**, 46-55.
25. A. M. Asiri, H. M. Marwani, S. B. Khan and T. J. Webster, *Int J Nanomedicine*, 2015, **10**, 89-96.
26. J. Yu, A. R. Lee, W. H. Lin, C. W. Lin, Y. K. Wu and W. B. Tsai, *Tissue Eng Part A*, 2014, **20**, 1896-1907.
27. P. Muniyandi, V. Palaninathan, S. Veerananarayanan, T. Ukai, T. Maekawa, T. Hanajiri and M. S. Mohamed, *Polymers (Basel)*, 2020, **12**.
28. E. Tomecka, M. Wojasinski, E. Jastrzebska, M. Chudy, T. Ciach and Z. Brzozka, *Mater Sci Eng C Mater Biol Appl*, 2017, **75**, 305-316.

29. P. J. Gouveia, S. Rosa, L. Ricotti, B. Abecasis, H. V. Almeida, L. Monteiro, J. Nunes, F. S. Carvalho, M. Serra, S. Luchkin, A. L. Kholkin, P. M. Alves, P. J. Oliveira, R. Carvalho, A. Menciacsi, R. P. das Neves and L. S. Ferreira, *Biomaterials*, 2017, **139**, 213-228.
30. N. Adadi, M. Yadid, I. Gal, M. Asulin, R. Feiner, R. Edri and T. Dvir, *Advanced Materials Technologies*, 2020, **5**, 1900820.
31. P. Martins, A. C. Lopes and S. Lanceros-Mendez, *Progress in Polymer Science*, 2014, **39**, 683-706.
32. C. Ribeiro, C. M. Costa, D. M. Correia, J. Nunes-Pereira, J. Oliveira, P. Martins, R. Gonçalves, V. F. Cardoso and S. Lanceros-Mendez, *Nat Protoc*, 2018, **13**, 681-704.
33. C. Ribeiro, C. M. Costa, D. M. Correia, J. Nunes-Pereira, J. Oliveira, P. Martins, R. Gonçalves, V. F. Cardoso and S. Lanceros-Méndez, *Nature Protocols*, 2018, **13**, 681-704.
34. M. M. Fernandes, D. M. Correia, C. Ribeiro, N. Castro, V. Correia and S. Lanceros-Mendez, *ACS Appl Mater Interfaces*, 2019, **11**, 45265-45275.
35. J. Nunes-Pereira, A. R. Silva, C. Ribeiro, S. A. C. Carabineiro, J. G. Buijnsters and S. Lanceros-Méndez, *Composites Part B: Engineering*, 2017, **111**, 37-44.
36. R. M. Meira, D. M. Correia, S. Ribeiro, P. Costa, A. C. Gomes, F. M. Gama, S. Lanceros-Méndez and C. Ribeiro, *ACS Applied Polymer Materials*, 2019, **1**, 2649-2658.
37. J. C. Dias, D. C. Correia, A. C. Lopes, S. Ribeiro, M. L. Jose, L. Vilas, L. M. Leo and S. Lanceros-me, DOI: 10.1007/s10853-016-9756-3.
38. D. M. Correia, L. C. Fernandes, P. M. Martins, C. García-Astrain, C. M. Costa, J. Reguera and S. Lanceros-Méndez, *Advanced Functional Materials*, 2020, **30**.
39. M. Demurtas, V. Onnis, P. Zucca, A. Rescigno, J. I. Lachowicz, L. De Villiers Engelbrecht, M. Nieddu, G. Ennas, A. Scano, F. Mocci and F. Cesare Marincola, *ACS Sustainable Chemistry & Engineering*, 2021, **9**, 2975-2986.
40. B. L. Gadilohar and G. S. Shankarling, *Journal of Molecular Liquids*, 2017, **227**, 234-261.
41. I. F. Mena, E. Diaz, J. Palomar, J. J. Rodriguez and A. F. Mohedano, *Chemosphere*, 2020, **240**, 124947.
42. A. Ferreira, J. G. Rocha, A. Ansón-Casaos, M. T. Martínez, F. Vaz and S. Lanceros-Mendez, *Sensors and Actuators A: Physical*, 2012, **178**, 10-16.
43. S. Ribeiro, R. M. Meira, D. M. Correia, C. R. Tubio, C. Ribeiro, C. Baleizão and S. Lanceros-Méndez, *Composites Part B: Engineering*, 2020, **185**, 107786.
44. J. Nunes-Pereira, P. Martins, V. F. Cardoso, C. M. Costa and S. Lanceros-Méndez, *Materials & Design*, 2016, **104**, 183-189.
45. R. Gonçalves, V. F. Cardoso, N. Pereira, J. Oliveira, J. Nunes-Pereira, C. M. Costa and S. Lanceros-Méndez, *The Journal of Physical Chemistry C*, 2018, **122**, 11433-11441.
46. R. Mejri, J. C. Dias, S. B. Hentati, M. S. Martins, C. M. Costa and S. Lanceros-Mendez, *Journal of Non-Crystalline Solids*, 2016, **453**, 8-15.
47. N. Slepickova Kasalkova, P. Slepicka, Z. Kolska and V. Svorcik, 2015, DOI: 10.5772/60824.
48. S. Bonetti, A. Pistone, M. Brucale, S. Karges, L. Favaretto, M. Zambianchi, T. Posati, A. Sagnella, M. Caprini, S. Toffanin, R. Zamboni, N. Camaioni, M. Muccini, M. Melucci and V. Benfenati, *Adv Healthc Mater*, 2015, **4**, 1190-1202.
49. Y. Yuan and T. R. Lee, *Contact Angle and Wetting Properties*, 2013.
50. T. Huhtamaki, X. Tian, J. T. Korhonen and R. H. A. Ras, *Nat Protoc*, 2018, **13**, 1521-1538.
51. B. Hermenegildo, R. M. Meira, D. M. Correia, A. G. Díez, S. Ribeiro, J. P. Serra, C. Ribeiro, L. Pérez-Álvarez, J. L. Vilas-Vilela and S. Lanceros-Méndez, *European Polymer Journal*, 2022, **171**, 111197.
52. C. A. Suarez Ruiz, J. Kwaijtaal, O. C. Peinado, C. van den Berg, R. H. Wijffels and M. H. M. Eppink, *ACS Sustainable Chemistry & Engineering*, 2020, **8**, 2441-2452.
53. M. V. Quental, M. Caban, M. M. Pereira, P. Stepnowski, J. A. Coutinho and M. G. Freire, *Biotechnol J*, 2015, **10**, 1457-1466.

54. D. M. Correia, L. C. Fernandes, C. García-Astrain, M. Tariq, J. M. S. S. Esperança, V. de Zea Bermudez and S. Lanceros-Méndez, *Composites Part B: Engineering*, 2019, **178**, 107516.
55. J. C. Dias, D. M. Correia, C. M. Costa, C. Ribeiro, A. Maceiras, J. L. Vilas, G. Botelho, V. de Zea Bermudez and S. Lanceros-Mendez, *Electrochimica Acta*, 2019, **296**, 598-607.
56. D. M. Correia, E. Lizundia, R. M. Meira, M. Rincon-Iglesias and S. Lanceros-Mendez, *Materials (Basel)*, 2020, **13**.
57. Í. F. T. de Souza, V. H. Paschoal, K. Bernardino, T. A. Lima, L. L. Daemen, Y. Z and M. C. C. Ribeiro, *Journal of Molecular Liquids*, 2021, **340**, 117100.
58. D. M. Correia, J. C. Barbosa, C. M. Costa, P. M. Reis, J. M. S. S. Esperança, V. de Zea Bermudez and S. Lanceros-Méndez, *The Journal of Physical Chemistry C*, 2019, DOI: 10.1021/acs.jpcc.9b00868.
59. J. F. Kiefer, J.; Leipertz, A. , *Applied Spectroscopy* 2007, **61**.
60. I. Rey, P. Johansson, J. Lindgren, J. C. Lassègues, J. Grondin and L. Servant, *The Journal of Physical Chemistry A*, 1998, **102**, 3249-3258.
61. R. Leones, C. M. Costa, A. V. Machado, J. M. S. S. Esperança, M. M. Silva and S. Lanceros-Méndez, *Electroanalysis*, 2014, **27**, 457-464.
62. D. M. Correia, C. M. Costa, E. Lizundia, R. Sabater i Serra, J. A. Gómez-Tejedor, L. T. Biosca, J. M. Meseguer-Dueñas, J. L. Gomez Ribelles and S. Lanceros-Méndez, *The Journal of Physical Chemistry C*, 2019, **123**, 27917-27926.
63. J. P. Serra, R. S. Pinto, J. C. Barbosa, D. M. Correia, R. Gonçalves, M. M. Silva, S. Lanceros-Mendez and C. M. Costa, *Sustainable Materials and Technologies*, 2020, **25**, e00176.
64. C. Ribeiro, J. P. Sissinen, V. t. Sencadas, V. t. Correia, S. Miettinen, V. P. Hytönen and S. Lanceros-Méndez, *Journal of Biomedical Materials Research - Part A*, 2015, **103**, 2172-2175.
65. H. Arzaghi, B. Rahimi, B. Adel, G. Rahimi, Z. Taherian, A. L. Sanati and A. Shiralizadeh Dezfuli, *Materials Advances*, 2021, **2**, 2231-2262.
66. A. Saberi, F. Jabbari, P. Zarrintaj, M. R. Saeb and M. Mozafari, *Biomolecules*, 2019, **9**, 448.